Dual-telescope multi-channel thermal-infrared radiometer for outer planet fly-by missions

Shahid Aslam,[a,*] Michael Amato,[a] Neil Bowles,[b] Simon Calcutt,[b] Tilak Hewagama,[a] Joseph Howard,[a] Carly Howett,[c] Wen-Ting Hsieh,[a] Terry Hurford,[a] Jane Hurley,[d] Patrick Irwin,[b] Donald E. Jennings,[a] Ernst Kessler,[e] Brook Lakew,[a] Mark Loeffler,[a] Michael Mellon,[c] Anthony Nicoletti,[a] Conor A. Nixon,[a] Nathaniel Putzig,[c] Gerard Quilligan,[a] Julie Rathbun,[f] Marcia Segura,[a] John Spencer,[c] Joseph Spitale,[f] Garrett West,[a]

[a]NASA, Goddard Space Flight Center, 8800 Greenbelt Rd., Greenbelt, MD, USA, 20771

[b]Atmospheric, Oceanic and Planetary Physics, Clarendon Laboratory, University of Oxford, Parks Rd., Oxford, UK, OX1 3PU

[c]Southwest Research Institute, 1050 Walnut St., Suite 300, Boulder, CO, USA, 80302

[d]RAL Space, Rutherford Appleton Laboratory, Harwell, Oxford, Didcot, UK, OX11 0QX

[e]Liebniz Institute of Photonic Technology, Albert-Einstein-Straße 9, Jena, Germany, 07745

[f]Planetary Space Institute, 1700 East Fort Lowell, Suite 106, Tucson, AZ, USA, 85719

Abstract. The design of a versatile dual-telescope thermal-infrared radiometer spanning the spectral wavelength range 8 to 200 μm, in five spectral pass bands, for outer planet fly-by missions is described. The dual-telescope design switches between a narrow-field-of-view and a wide-field-of-view to provide optimal spatial resolution images within a range of spacecraft encounters to the target. The switchable dual-field-of-view system uses an optical configuration based on the axial rotation of a source-select mirror along the optical axis. The optical design, spectral performance, radiometric accuracy, and retrieval estimates of the instrument are discussed. This is followed by an assessment of the surface coverage performance at various spatial resolutions by using the planned NASA Europa Mission 13-F7 fly-by trajectories as a case study.

Keywords: dual-telescope, dual-field-of-view, filter radiometer, icy moons, thermal emission, surface temperature, Europa.

***Shahid Aslam**, E-mail: shahid.aslam-1@nasa.gov

1 Introduction

A major challenge for thermal-infrared radiometer imaging instruments on fly-by missions to the outer planets, icy moons and primitive bodies in the solar system is to make high-fidelity thermal emission measurements of the target at large distances while retaining the ability to also make measurements when at closest approach. In an ideal case, the instrument would employ a telescope able to zoom continuously between field-of-view limits commensurate with science requirements. However, complexities in zoom mechanisms introduce additional risks and failure modes. A low risk solution that achieves fly-by mission science goals is to use a dual-telescope system that has two fields-of-view that are switchable. The wide-field-of-view (WF) or low magnification mode is used for observing a large scene area and searching for possible interesting features. The narrow-field-of-view (NF) or high magnification mode is then used for close-up recognition and identification ("zooming-in"). The two modes significantly enhance the effectiveness of a radiometer imaging system by providing two distinct operating modes that will

enable reconnaissance and science objectives over a greater portion of the trajectory than with the use of a single telescope tuned to a specific field-of-view.

Infrared (IR) spectrometers and radiometers have flown previously on fly-by trajectories of the outer planets [1,2,3,4], but all these instruments had fixed-telescope aperture diameters; for example, Cassini/CIRS uses a 50-cm diameter telescope, which allows for a 16-fold field reduction from similar IR spectrometers flown previously on Earth- and Mars-orbiting spacecraft [5,6,7]. With this telescope, Jupiter filled the field-of-view (FOV) approximately four weeks before Voyager's closest approach. More recent thermal radiometers *e.g.* Mars Climate Sounder on MRO [8], Diviner on LRO [9] and MERTIS on Bepicolombo [10]) with fixed FOVs were designed for optimal spatial resolution from an orbiting spacecraft.

Future multi-year tours of the outer planet systems - and to the gas giants in particular, with many choreographed fly-by trajectories of their icy moons - will require a number of changes to earlier radiometer instrument designs: (i) an optimization of the fields-of-view in order to maximize surface data coverage at various spatial resolutions from farthest to closest approaches; (ii) a reduction in the noise equivalent spectral radiance (NESR) of the instrument by using higher sensitivity detectors and low-noise radiation-hard readout electronics; (iii) a reduction of the thermal background radiation contribution by operating the instrument at an optimal temperature; (iv) careful consideration to the number and band passes of the spectral channels in order to uniquely determine the surface temperature and emissivity of the surface under investigation; and (v) attention to radiation-hardening of the instrument and electronics to ensure proper operation in high-energy and high-fluence particle environments (*e.g.*, Jovian magnetosphere).

The dual-telescope multi-channel thermal-infrared radiometer concept described here evolved out of a series of thermal instrument concept studies that, collectively, addressed all of the concerns above: in particular, "Jupiter Europa Thermal Sounder," for the NASA-led Jupiter Europa Orbiter (JEO) of the Europa Jupiter System Mission (EJSM) in 2011 [11]; "Oxford RAL Terahertz-Infrared Sensor (ORTIS)", a composite IR/THz instrument that was proposed for the ESA Laplace Mission [12], subsequently renamed JUpiter ICy moons Explorer (JUICE); which then, by dropping the THz capability ORTIS evolved into the "Jupiter System Thermal Infrared Mapper (JSTIM)", which was proposed for the ESA-led JUICE Mission call in 2012 [13]. Continuing studies evolved JSTIM into the "Thermal Imager for Europa Reconnaissance (TIMER)", a NASA-funded instrument concept in 2013 [14]; which then with maturation and risk mitigation studies subsequently developed into the "Thermal Imager for Europa Reconnaissance and Science (TIMERS)", which was proposed for the NASA-led Europa Mission announcement opportunity call in 2014 [15].

Although, the TIMERS instrument, designed specifically for thermal-infrared emission measurements from Europa's surface, was not selected in May 2015 as part of the science instruments suite on NASA's Europa Mission it still remains a highly versatile thermal instrument for inclusion on-board future fly-by missions to icy planets, bodies and satellites. In this paper, a brief description of how thermal emission measurements from icy surfaces help characterize thermo-physical properties is given followed by a discussion on the optical and electronic readout design, radiometric performance and accuracy of the evolved dual-telescope TIMERS concept, hereon called the thermal radiometer; an assessment is given of the thermal radiometer performance, of the surface coverage at various spatial resolutions that can be attained, by using the planned Europa Mission 13-F7 fly-by trajectories [16] as a case study; and finally an example of how the dual telescope design will provide observations at multiple scales.

The thermal radiometer's WF and NF telescopes and filter channels, described here, are specifically optimized for multiple Europa fly-by's, in which the farthest approach is 60,000 km and the closest approach is 25 km. The thermal radiometer filter channels are optimized for measuring Europa's surface temperature in the range of 53-135 K, with a noise equivalent temperature difference (NETD) of ≤2 K, using five spectral pass bands, 8-14 μm, 12.5-25 μm, 25-50 μm, 50-100 μm and 100-200 μm, defined by a combination of filters and windows. The reflected solar radiation contextual information is derived from a bore-sighted visible-near infrared camera as part of the mission payload, or alternatively if this capability is not available then the 100-200 μm channel can be replaced with a solar channel (0.35-2.8μm).

For fly-by missions to other planetary targets, the WF and NF telescope fields-of-view can be appropriately resized for optimal spatial resolution, coverage and radiometric performance specific for the planned fly-by trajectories; if required the NF telescope can be descoped, resulting in a lower-mass instrument while maintaining high-fidelity thermal imaging and signal-to-noise ratio (SNR) performance; albeit with less flexibility in the ability to gather higher spatial resolution data from a distance. Furthermore, the filter channel specifications can easily be changed, to accommodate the shift in planetary Planck function peak as a function of target temperature, since the filter assembly is at an intermediate focus in the optical system.

The thermal radiometer described here will have particular relevance to future Flagship Missions (*e.g.*, Uranus and Neptune or Enceladus [17]) and potential New Frontiers Missions (*e.g.*, Io Mission [18] or Trojan Asteroids [17]).

2 Planetary satellite surfaces

For satellite science, judiciously selected bands in the 8-200 μm spectral range provides sensitivity to sub-pixel temperature variations since the 53-135 K Planck function inflection points are optimally bracketed as shown in Fig. 1. In contrast to devices with purely sub-mm bands, which do not fully sample the inflection points in this temperature range, a thermal radiometer can easily detect and characterize sub-pixel temperature variations, including small, unresolved endogenic hot spots. In addition, the broad wavelength coverage means that it is more suited for mapping surface thermo-physical properties and composition than a sub-mm device focused on a very narrow range of frequencies and a single FOV.

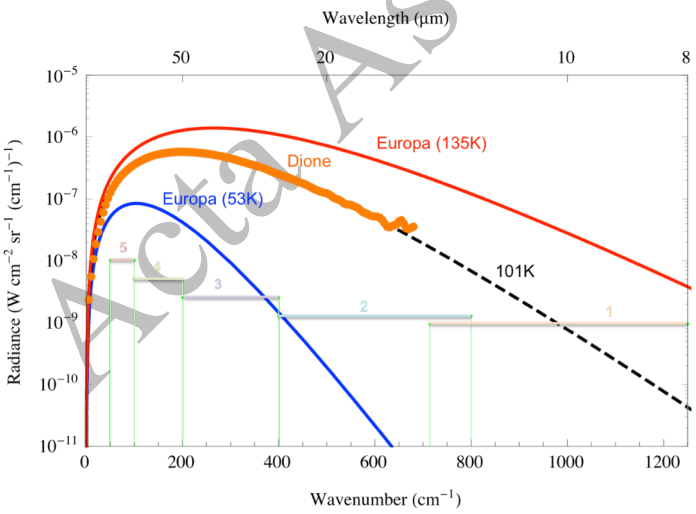

Figure 1. Measured radiance spectrum of Dione (Cassini/CIRS) together with estimated dayside/night-side spectra of Europa and location of radiometer IR filter band channels.

The wavelength coverage and high spatial resolution is also ideally suited for measuring the endogenic heat flow and volcanic activity (*e.g.* from Io), as it is also sensitive to the shorter wavelength radiation associated with Io's hotter volcanic thermal emission.

Characterization and comparison of the surface properties of the major satellites of the outer planets will provide key information on their formation and evolution and could provide unique discoveries of any near-surface heat sources, *e.g.,* the 'tiger stripes' of Enceladus [19] and thermal contrasts associated with surface-magnetosphere coupling and other processes (*e.g.,* the 'pacman' of Mimas [20]).

3 Measurement Principle

The radiometer measures thermal-infrared emission from a surface over wavelength bands in the spectral region 8 to 200 μm. Assuming an atmospheric transmittance of unity, the radiance at the detector, $L_d(\lambda, T)$, within the spectral range λ_0 (shortest wavelength) and λ_n (the longest wavelength), from a gray body at temperature T is given by Planck's function [21] modified by surface emissivity and instrument response is given by:

$$L_d(\lambda, T) = \int_{\lambda_0}^{\lambda_n} \tau(\lambda)\varepsilon(\lambda) \frac{2hc^2}{\lambda^5(e^{hc/\lambda kT}-1)}\, d\lambda \qquad [\mathrm{Wm^{-2}sr^{-1}\mu m^{-1}}]$$

where $\tau(\lambda)$ is the radiometer's spectral transmittance, $\varepsilon(\lambda)$ is the target's spectral emissivity, h is Planck's constant, c is the speed of light, k is Boltzmann's constant. If the functional form of $\varepsilon(\lambda)$ is known within an unknown constant term, measurement's of radiance in at least two thermal spectral wavelength bands can be used to directly determine the surface temperature and emissivity at a range of spatial resolutions depending on the range of the spacecraft to the targets surface.

Surface temperature and emissivity can further be used to constrain the thermo-physical properties of the surface, such as thermal inertia (T) which is a measure of how the surface responds to solar insolation and is dependent on the thermal conductivity, $\kappa(T)$, density, ρ, and specific heat capacity, c_s, given by $\mathrm{T} = \sqrt{\kappa\rho c_s}$. For a small thermal inertia ($\mathrm{T} < 30$ $\mathrm{Jm^{-2}K^{-1}s^{-1/2}}$), the surface temperature changes very rapidly to a change in insolation, while for a large thermal inertia ($\mathrm{T} > 500$ $\mathrm{Jm^{-2}K^{-1}s^{-1/2}}$) the surface temperature change is much slower.

These measurements help to establish surface temperatures and thermo-physical properties of icy moons, aid in characterizing potential landing sites, and establish day- and night-time multi-wavelength temperature maps. The diurnal surface temperature variations mapped can be used to understand surface volatile stability, look for endogenic heat sources, and to map thermal inertia, which can be related directly to physical properties of the surface such as density and composition. With constraints on the surface albedo (from a visible imager), single daytime temperature measurements can be used to model a surface thermal inertia [22]. In cases where constraints on surface albedo are not available, overlapping measurements of daytime and nighttime temperatures can be used in concert to model the surface thermal inertia, the surface albedo and heat flow [23, 24, 25]. Spectral emissivity variations can also be detected by comparing the broadband surface emission spectra seen with blackbody curves, providing additional constraints on surface composition and water ice grain size.

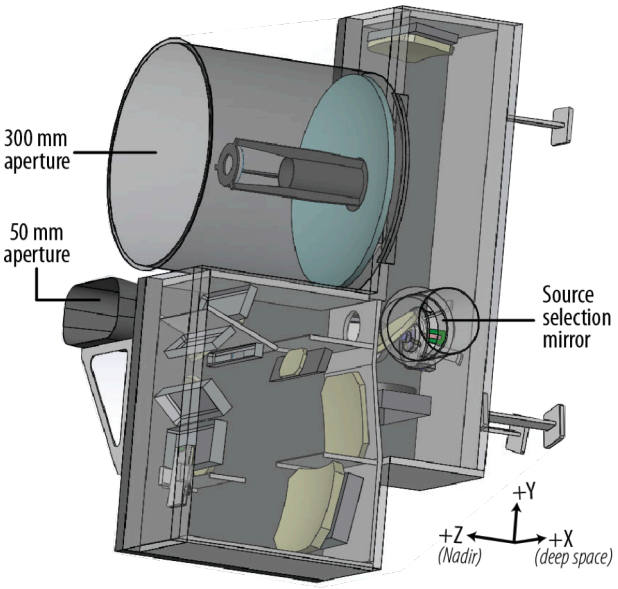

Figure 2. Radiometer concept showing the 300 mm NF telescope and the port that enables the instrument to directly view targets with its smaller, fully radiometrically-calibrated 50 mm WF telescope system by means of a source select mirror.

Table 1. Dual-telescope radiometer specifications.

Parameter	Property	
Target Temperature	50 to 300 K	
Temperature Accuracy	≤2 K	
Spectral Range	8-to-200 μm in five distinct spectral channels	
Detector Type	Thermopile	
Detector Format	(5×64) pixel array	
Pixel Size	250 μm x 250 μm	
F-number	f/#2 at image plane	
Etendue (AΩ)	1.23×10^{-8} m^2 sr	
Telescope	Narrow Field	Wide Field
Aperture Size	300 mm	50 mm
Detector Pixel iFOV	0.42 mrad	2.5 mrad
Resolution @ 60,000 km	25 km	150 km
Resolution @ 100 km	84 m (2-pixel bin)	250 m
Mass	~9.4 kg (without harness)	
Science Power	~8.7 W	
Observation Strategy	Nadir pushbroom mapping	

4 Instrument Overview

The dual-telescope thermal radiometer is designed specifically for a Europa Mission, shown schematically in Fig. 2, with key specifications summarized in Table 1, uses a custom 5-line 64 pixel thermopile array (5×64) chip manufactured by the Institute of Photonic Technology (IPHT) in Germany [26]. Each of the five (1×64) linear subarrays is a unique channel defined by miniature filters matching the bands shown in Fig. 1, are placed at an intermediate focus. The 5-line arrays are scanned in a "push-broom" manner across the target body to build up thermal maps. Key Focal Plane Assembly (FPA) components are the Multi-Channel Digitizer Application Integrated Specific Circuit (MCD ASIC) readout [27, 28] and the thermopile array chip. To achieve adequate Signal-to-Noise Ratio (SNR) (in part by pixel averaging) and spatial resolution when viewing a cold target from 60,000 km, the instrument uses a NF telescope with a 300 mm aperture. When viewing the target at closer approaches, the instrument switches to a "zoomed-out" WF telescope with a 50 mm aperture, at lower spatial resolution. This provides versatility in the ability to study specific features that merit finer image detail. Furthermore, the WF will mitigate against beam smear due to high (~4 km/s) ground-track velocities near closest approach. The switching is achieved by using a source select mirror (Fig. 3) that is used to gather light from: 1) the target body via a fold mirror, *i.e.* the smaller WF telescope, 2) the target body via the larger NF telescope, 3) a blackbody calibrator, or 4) deep (cold) space. Switching between the fold mirror, NF telescope and in-flight calibration requires a mechanism. The source select mirror mechanism fail-safe position is designed to point at the target body via the fold mirror. The near-collimated output from the NF telescope ensures alignment with respect to the remaining optics without tight tolerances, greatly simplifying the optical design.

5 Optical Design

The radiometer optical system (Fig. 3) is comprised of a NF three-mirror afocal telescope with a 300 mm primary aperture, a WF telescope with a 50 mm aperture, a filter assembly, a three-mirror astigmatic (TMA) image relay and a detector focal plane.

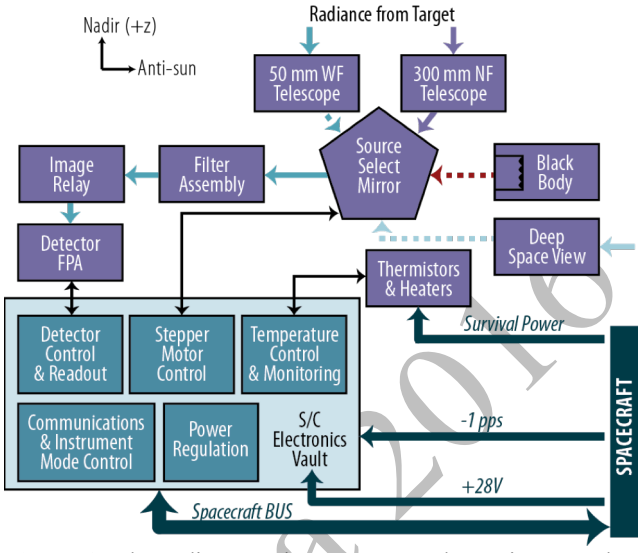

Figure 3. The radiometer has a source select mirror used to view targets directly using the NF or WF telescope. It is also used to view deep space and an internal blackbody to fully radiometrically calibrate the instrument - an essential requirement for a filter channel radiometer.

5.1 Dual-Telescope Design

Both telescopes have the role of collecting visible to far-infrared light and share an optical path beyond the source select mirror to the focal plane assembly. The NF telescope (Table 2) is an afocal, three-mirror system (and a fold mirror) designed to provide a 6× de-magnified pupil at the entrance pupil of the WF telescope. A source select mirror is placed at the exit pupil of the NF telescope and uses a mechanical mechanism to re-direct light from the output of the NF telescope into the entrance pupil of the WF telescope. The WF telescope is a reflective unobscured version of a Petzval lens, a type commonly used for wide-angle reconnaissance missions, (*e.g.* TIRS/LandSat 7, [29]). When using the WF telescope the source select mirror is rotated to point directly at the target body via a fold mirror, bypassing the NF telescope assembly. Light entering the WF telescope is focused onto a filter assembly and then relayed onto the detector plane. The image relay sub-system is a finite-conjugate TMA design with a reduction ratio of 2 and an image space F/# of 2. The optical design (Fig. 4) successfully balances image quality performance within the demanding FOV. The surface curvatures and aperture dimensions for optics have been modified to accommodate the instrument's unique FOV, aperture, and image requirements.

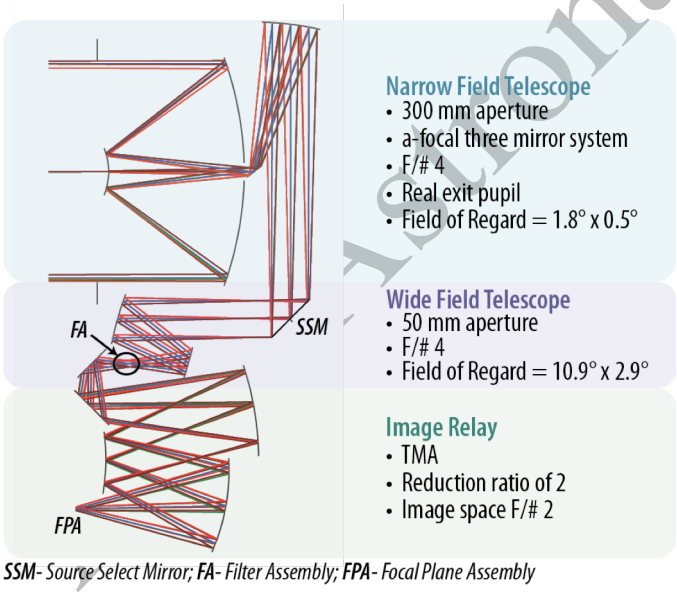

Figure 4. A ray trace of the optical design showing how the source selection mirror (SSM) takes light from the NF or the WF telescope and images it on filters. The image relay reduces the image at the filter assembly onto the detector FPA by a factor of two. The SSM turns into the page to look out of the 50 mm baffle via a fold mirror.

Table 2. First-order optical specifications of NF and WF telescopes.

Property	NF	WF
Aperture	300 mm	50 mm
Field of View cross track x along track	1.81°×0.024°	10.87°×0.14°
Telescope F/#	4	4

5.2 Filters and Windows

The radiometer's five spectral channels are defined using individual miniaturized spectral bandpass filters in combination with long and/or short wavelength blocking windows (Table 3). Channels 1 and 2 use thin film interference filters on zinc-sulphide (ZnS) substrates and germanium (Ge) respectively. Ge, and ZnS have robust mechanical and thermal properties and high optical transmission at 170 K [30, 31], within their respective channel bandpasses. Channels 1 and 2 employ salt (KCl and NaCl) windows for long-wave blocking. Channel 3 has an interference filter to limit the overall bandpass, and Channels 4 and 5 each have an absorbing quartz filter for short-wavelength blocking. All channels have a field-limiting aperture in front of filter-window stacks that runs the length of the detector array and limits the in-track FOV. The individual filters are mounted in a metal filter assembly located at an intermediate focus in the optical system (Fig. 4). Filters placed at an intermediate focus in the optical train are preferred over filters mounted directly on top of the detectors since this (i) avoids complications due to optical cross-talk that arises from both reflections and emissions from the detector elements reflected back from the filter surface causing FOV side lobes; and (ii) avoids spectrally-dependent FOV effects that arise from scattered light from the meshes re-entering the field of view via the filter support structure. Filter assembly thermal stability (± 0.1 K) is important [32] to prevent changes in thermal properties. Since the thermopile arrays in the detector focal plane assembly are sensitive to all wavelengths that irradiate on the gold black absorber (low reflection), small excursions in the temperature of the filters will produce measurable signals, because the filters are sources of blackbody radiation at all wavelengths away from their narrow spectral windows. Temperature changes in the filters due to the changing background temperature are potentially large enough to cause a measurable, but spurious, effect. Therefore, the filter assembly is mounted in good thermal contact onto a mount that is thermally-coupled to the optical bench, ensuring that the filter assembly and the optical bench are at the same temperature. The filter assembly incorporates aluminum alloy baffles between the line arrays of the filters to reduce transmission of off-axis rays produced from reflections within the instrument housing.

Table 3. Spectral channels use both windows and filters. The filter spectral band passes are optimized to capture the target's surface temperatures between 50 K and 300 K.

Ch	Spectral Bandwidth (μm)	Window Short Blocking	Window Long Blocking	Substrate	Filter Type
1	8-14	-	NaCl	ZnS	Film
2	12.5-25	-	KCl	Ge	Film
3	25-50	Interference filter on silicon substrate		Polypropylene	Film and Mesh
4	50-100	Quartz	-	Polypropylene	Mesh
5	100-200	Quartz	-	Polypropylene	Mesh

6 Detectors Focal Plane Assembly

Key components to the detector FPA, Fig. 5, are the thermopile array and MCD ASICs. An IPHT 5-line (5×64) thermopile array chip is used for the sensing pixels at the FPA. A representative (1×64) array chip has been tested with 17 MeV electron irradiation to a total ionizing dose (TID) of 6 Mrad (Si), without any change in the pixels' electrical resistances [33]. IPHT thermopiles on REMS/MSL have been successfully tested at 138 K at Astrium Crisa [34].

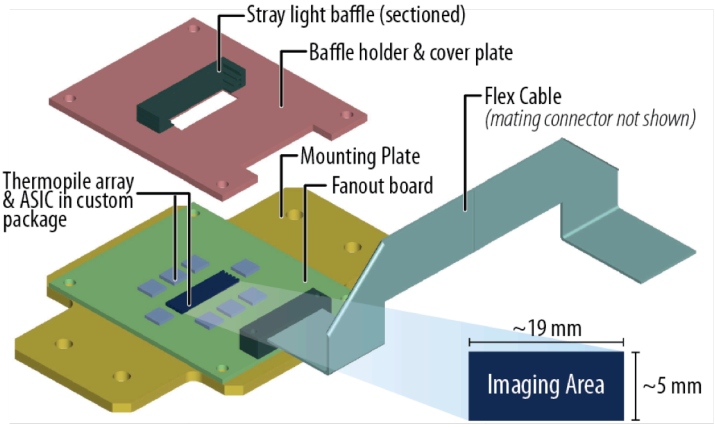

Figure 5. Schematic of the detector FPA showing the layout of the 5-line 64 pixel thermopile array chip and the integrated MCD ASICs for low-noise readout.

The MCD ASICs are also radiation-hard, having been tested to 53 Mrad (Si) TID and an effective linear energy transfer of 174 MeV-cm^2/mg with no single event latchup (SEL) events [28]. The ASIC was also successfully operated at 153 K at NASA, GSFC. The FPA is powered by several Kelvin-sensed pairs, providing a filtered 1.8 ± 0.1 V supply voltage to all ASICs, and by multiple ground connections, several of which are also Kelvin-sensed. The total supply current for the FPA pixel circuitry is less than 400 mA. The thermopile pixels and ASIC digitizers are referenced to a vault-generated common mode voltage (VCM), which is Kelvin-sensed.

Each ASIC digitizes 40 image pixels and streams the data over eight low voltage differential signaling (LVDS) pairs back to the spacecraft (S/C) vault. Included in these data streams are thermistor-generated FPA temperature data. Control and housekeeping tasks associated with the ASICs are provided by five LVDS serial peripheral interface signals connecting the S/C vault to the FPA. These signals are: serial data input (SDI), serial data output (SDO), serial clock (SCK), serial load (SLD) and chip select (CS). The SDI interface speed is no higher than 200 kHz. The ASICs' internal clocks are derived from a vault-based, crystal-referenced LVDS clock signal, which is nominally at 1 MHz frequency with 50% duty cycle, but can be varied from 500 kHz to 4 MHz. This clock is used to generate the ASICs' internal chopper and analog digital converter (ADC) clock rates.

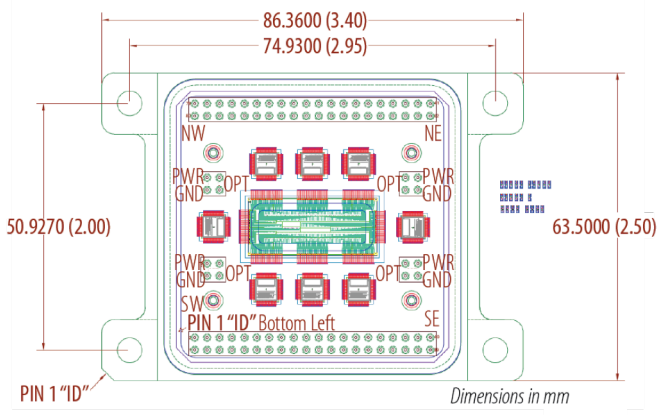

Figure 6. Thermopile array chip and MCD ASICs are hybridized in a custom package.

6.1 Thermopile array chip

The FPA detector chip has five rows of high sensitivity linear thermopile array (5×64) pixels in a push-broom configuration. Fig. 6 shows the conceptual layout of the proposed thermopile array in a custom package that also houses the MCD ASICs. Each pixel in the array consists of a floating low-stress, silicon-nitride (Si-N)

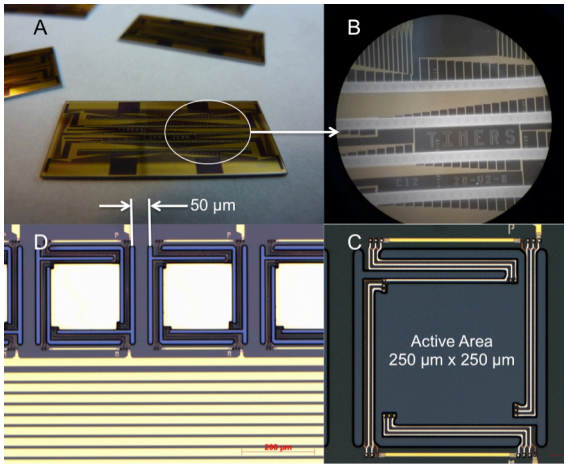

Figure 7. Geometry and arrangement of the 5-line 64-pixel thermopile array chip. (A) IPHT manufactured thermopile pixel floating membranes on one chip using bulk micromachined silicon; (B) close-up of pixels; (C) 250 µm square pixel with demonstrated D^* of 1.37×10^9 cm√Hz/W and 64 ms thermal time constant; (D) pixel layout of one line showing pixel separation.

gold wire bond per detector pixel. An electronic chopping circuit modulates the DC voltage signal from each thermopile pixel. The resulting AC signal is amplified, demodulated, and integrated, then multiplexed into an ADC. Because the *1/f* noise is translated to harmonics of the chopper clock frequency, the *1/f* noise in the Complimentary Metal Oxide Semiconductor (CMOS) amplifier is dramatically reduced. Integrated signals from each of the 320 pixels are multiplexed into eight digital output streams. The thermopile pixel elements have a typical electrical resistance of ~5 kΩ at 170 K and are dominated by Johnson noise (*i.e.* ~7 nV/√Hz). The input-referred noise for the MCD ASIC at 170 K is ~ 15 nV/√Hz, and when these noise sources are added together with the bit noise in quadrature then the overall system noise is 16.5 nV/√Hz. This represents a system D^* of 5×10^8 cm√Hz/W, which meets the sensitivity requirement with margin. The detector FPA support structure has enough thermal inertia to ensure a stable thermal environment for the array and MCD ASICs.

membrane with bismuth-antimony (Bi-Sb) thermocouples connected in series. A two-line 15-pixel thermopile array with a specific detectivity (D^*) of 1.3×10^9 cm√Hz/W for each pixel, is integrated on the Mercury Radiometer and Thermal Infrared Spectrometer (MERTIS) on BepiColombo due to launch in early 2017 [10]. The thermopile array requirements for the radiometer concept proposed here are given in Table 4. A manufactured 5-line thermopile array chip is shown in Fig. 7 which demonstrates a pixel D^* of 1.37×10^9 cm√Hz/W and 64 ms thermal time constant. These detectors have silver black as the absorber. For flight the detector pixels will be coated with gold black, which has high absorption and a nearly flat spectral response from 8-to-200 µm [35]. The D^* requirement (Table 4) is in the 10 Hz range, therefore low *1/f* noise in the detectors and readout circuitry is essential. Each MCD ASIC is connected to the thermopile array with one

Table 4. Thermopile array parameters.

Detector Array Parameter	Value
Manufacturer	IPHT (Jena, Germany)
Detector Type	Thermopile Array
Detector Material	Bi-Sb
Design Waveband	8-to-200 µm
Pixel Count	5×64
Pixel Pitch	300 µm (cross-track) 1500 µm (in-track)
Pixel Size	250 µm×250 µm
Responsivity	≥340 V/W
Dynamic Range	250 K (50 K to 300 K)
Thermal Time Constant	≤100 ms (-3 dB cut-off)
Absorber	Gold black
D* (10 Hz, 8-200 µm)	>5×10^8 (goal: >1 x 10^9) cm√Hz/W
Radiation Hardness	>6 Mrad (Si) TID
Operating Environment	Vacuum
Operating Temperature	170-to-300 K
Survival Temperature	150-to-384 K

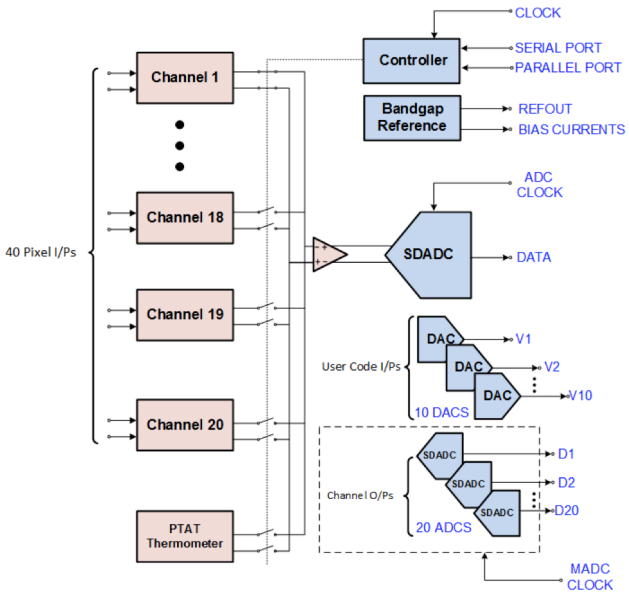

Figure 8. MCD ASIC block diagram.

high input impedances) while the DT aspect combines chopper and correlated double sampling (CDS) techniques. Each channel's back-end utilizes a DT integrator, which averages the amplified signals and attenuates Johnson noise, in addition to providing additional gain. Fig. 9 provides a plot of integrator gain vs. frequency for a chopper clock period of 4 µs. Each channel's output connects to its own SDADC or via a multiplexer to one SDADC. Having a dedicated SDADC for each channel allows for very long integration times by averaging each channel's output over the required interval. The multiplexed SDADC is useful for shorter integration times and saves power since the channel SDADC's can be powered down.

The ASIC uses a single input clock (~1.0 MHz) to generate all on-chip control signals, such as the chopper/CDS clocks, the integrator time constants and the SDADC conversion clock. The SDADC uses a second-order modulator with differential inputs. The MCD ASIC has successfully passed its functional, performance, radiation [28] and cold tests. A summary of the MCD ASIC specifications in given in Table 5. A plot of V_{out} *vs* V_{in} for one channel measured before and after 53 Mrad (Si) of TID is shown in Fig. 10.

The baseline FPA is comprised of a 5×64 thermopile array that outputs simultaneous analogue

6.2 MCD ASICs

GSFC has designed and built a custom radiation-hardened-by-design (RHBD) 180 nm CMOS ASIC for thermopile readout that has immunity to SEL at 174 MeV-cm^2/mg and 53 Mrad (Si) TID. The MCD ASIC (Fig. 8 and inset of Fig. 9) has 40 low-noise pixel amplifier channels with configurable gain/filtering that are digitized by on-chip 16-bit sigma delta ADCs (SDADC).

Each channel uses a combination of continuous time (CT) and discrete time (DT) signal processing to amplify the thermopiles' microvolt level signals with low *1/f* and thermal noise. The CT portion of the channel provides high gain using instrumentation amplifier topology (with

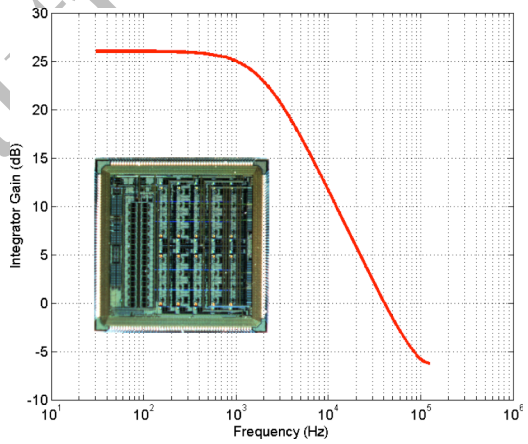

Figure 9. Discrete time integrator frequency response for t_{chop} = 4 µs; inset shows a MCD ASIC die (5 mm × 5 mm).

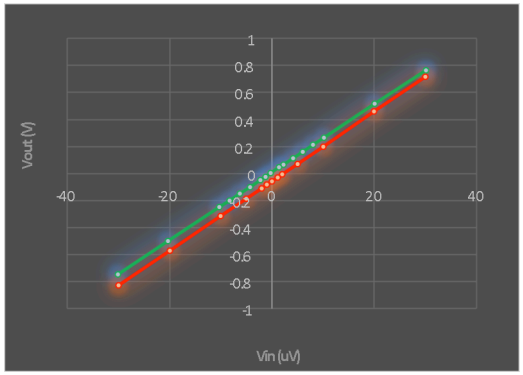

Figure 10. Gain before (green) and after (red) 53 Mrad (Si) gamma-ray TID.

Table 5. MCD ASIC specifications.

Parameter	Value	Comments
Chip size	5 mm x 5 mm	180 nm CMOS
Supply voltage	1.8 ± 0.1V	
Supply current	10 mA @ ~153 K 40 mA @ ~300 K	Programmable with an input bias current
Number of pixel channels	40	High gain variable
Number of housekeeping channels	2	Low gain variable
Interface	Parallel/SPI/LVDS	User selectable
SNR ratio (Vin = 50μv)	200	User defined integration time
Nominal Gain	200 - 2000	Combination of CT/DT gain
Integration Time	1 ms – 1 s	User defined
Chopper frequency	64 – 256 kHz	User defined
ADC resolution	12 – 16 bits	User defined
ADC conversion rate	4 kHz	User defined
ADC clock rate	500 kHz – 4 MHz	User defined

voltages from a total of 320 pixels. Eight 40-channel MCD ASICs are used to digitize all 320 pixels. The ASICs are distributed between the array outputs in groups of two or three ASICs per line of 64 pixels (Fig. 11). This approach adds partial redundancy to the FPA readout function, with a minimum of 24 pixels from each line array still available even if one ASIC is off-line. For example, line array 1 is digitized by ASIC1, ASIC2 and ASIC3, while line array 3 is digitized by ASIC4 and ASIC8 as shown in Fig. 11. The channels have self-calibration capability so that any gain mismatches between channels and ASICs can be stored and translated to correction coefficients in the MEB controller.

An additional two channels in the ASIC can be used for housekeeping tasks such as supply current measurement or thermistor-based temperature measurement for FPA temperature readout back to the vault; a thermistor bias current is provided by the MCD. The user can also use the on-chip bandgap based PTAT (Proportional To Absolute Temperature) voltage source for ASIC temperature measurement.

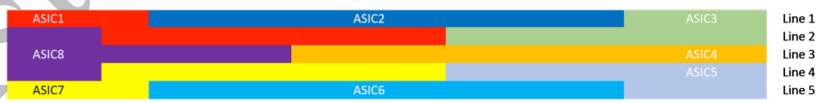

Figure 11. Thermopile - ASIC allocation (each color represents the pixel allocation to an ASIC).

The MCD ASIC provides both a parallel and a serial-parallel interface (SPI) for controlling all aspects of the chip and sending back digitized data to the vault. The data is returned via an LVDS interface at rates up to 4 MHz. The ASIC clocks inputs are also LVDS compatible.

The MCD ASIC was tested over a range of temperatures extending down to 153 K and showed improved performance (*e.g.* supply current requirements dropping to 25% of nominal) at cold temperatures, as predicted in the design simulations.

7 Expected Instrument Performance

7.1 Spectral Performance

The radiometer's channel spectral responses are determined by a combination of interference filters, dielectric mesh filters, and blocking windows located at an intermediate focus within the

optical train. The baseline filter set is shown in Table 3. The locations of these spectral channels in relation to representative blackbody curves are shown in Fig. 1.

Table 6. Calculated NESR and SNRs from baseline filter set shown in Table 5 when viewing a blackbody at 50 K, 85 K, 130 k, and 170 K for an integration time of 1s.

Channel #	Δλ (μm)	Δν (cm^{-1})	NESR (nW cm^{-2} sr^{-1} $(cm^{-1})^{-1}$)	SNR			
				50 K	85 K	130 K	170 K
1	6	535.72	0.76	0	0.6	70	646
2	12.5	400	1.01	0.1	27	523	2173
3	25	200	2.36	6	136	760	1741
4	50	100	5.40	18	109	304	512
5	100	50	10.81	10	32	64	95

D* is assumed to be 1 x 10^9 cmvHz/W, with detector area of 6.25 x 10^{-4} cm^2 and a system throughput of 0.5.

7.2 Radiometric Sensitivity

The baseline instrument uses thermopile detectors with a Noise Equivalent Power (NEP) of 2.5 x 10^{-11} W/√Hz. Combined with the instrument etendue ($A\Omega$), spectral bandwidth, and expected system and optical efficiencies, the Noise Equivalent Spectral Radiances (NESRs) and the SNRs for temperatures of 50 K and 135 K for each of the five filter channels has been calculated using an integration time of 1s, as shown in Table 6. Using the calculated NESRs, the NETD in a single pixel (Fig. 12) when viewing scene temperatures up to 300 K is computed for an observation time of 1s. The NETD performance shows that the radiometer can resolve a 2 K temperature contrast over the temperature range of improved by integrating for longer than 1s at observing distances where <1 pixel smear is achievable (§7.4). For a dwell time of 0.1s, the NETD for all channels increase by √5, giving better than 2 K NETD for channels 1 to 4 and ~5 K NETD for channel 5.

7.3 Radiometric Accuracy

Measured radiances depend on both offset and gain uncertainty as a function of time [36]. The offset uncertainties during flight arise due to thermopile detector and front-end electronic readout noise plus uncertainties in the interpolation of signals from the on-board calibration blackbody and cold space interrogated at known time intervals. While the detector system is well characterized prior to integration, final assessment of the interpolation uncertainty can only be formulated when the instrument undergoes thermal-vacuum testing that simulates environmental conditions. It is expected this uncertainty will be at the level of the thermopile detector noise at the output of the signal chain. This is the dominant uncertainty when looking at cold space. The gain uncertainty is the combination of the on-board blackbody temperature measurement, non-uniformity of the blackbody surface, detector, and electronics noise, and the interpolation between points at different blackbody temperatures. This gain uncertainty is calibrated and removed during flight by performing intermittent views of the on-board calibration blackbody and cold space. The instrument's blackbody calibration is designed to achieve an end of life accuracy of 0.1 K,

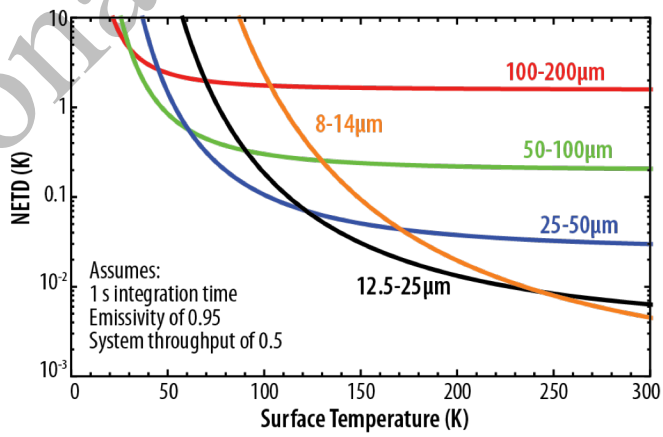

Figure 12. NETD for thermal channels shows the instrument will resolve temperature contrast below 2 K in temperature range 50 K to 170 K. For 0.1s integrations multiply NETD by √5.

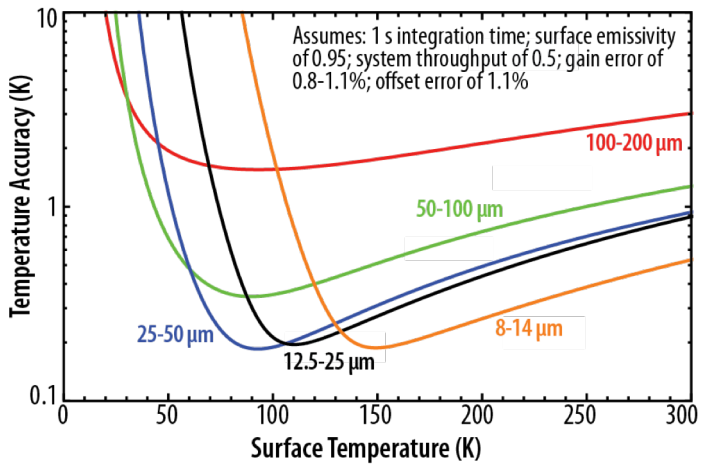

Figure 13. Calculated temperature accuracy as a function of surface temperature. For 0.1s integrations multiply temperature accuracy by √5.

traceable to National Institute of Standards and Technology. Using this calibration scheme, a radiometric accuracy of better than 2 K and/or 10% of the measured signal will be achieved. The calculated surface temperature accuracy is shown in Fig. 13.

7.4 Retrieval Estimates

The surface temperature retrieval error in the different channels depends both on the radiometer's noise performance and also on the rate of change of the Planck function with temperature, which itself varies hugely with temperature and wavelength. However, the instrument's ability to determine thermo-physical quantities, such as thermal inertia and albedo, is constrained by more factors than just SNR. In particular, accuracy is limited by the time-of-day coverage, and perhaps also by angular coverage (capturing emission radiated in all directions by the surface). The ability to distinguish endogenic heat flow will rely on accurate modeling of absorbed sunlight, established using bore-sighted visible and near infrared photometry at the same pixel resolution, and models to account for its angular variation.

The radiometer's wide thermal spectral range, which covers both sides of the Planck function peak for typical temperatures modeled on icy moons, can easily differentiate between two temperature regions in a single pixel. Fig. 14 shows the position of the broad pass band filters with the predicted spectrum when 90% of the FOV views cool temperatures (75 K) and 10% views hot temperatures (140 K).

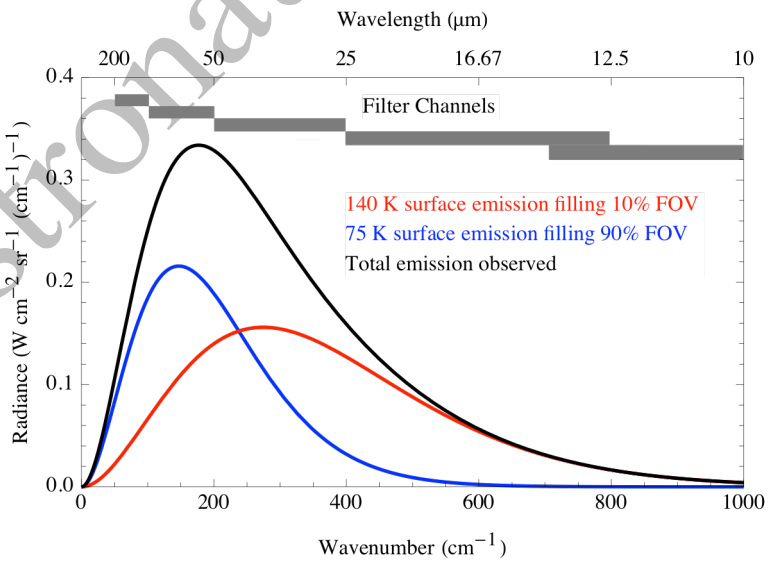

Figure 14. Filters are able to accurately view both cold and hot temperatures concurrently, as shown by the calculated spectral radiance of a surface where 90% is at 75 K and 10% at 140 K.

7.5 Spatial Resolution and Nadir Pointing

The NF and WF modes have a pixel instantaneous FOV (iFOV) of 0.42 mrad and 2.5 mrad, respectively. The projected NF and WF iFOV on a target's surface throughout a typical fly-by

trajectory, from 60,000 km to 25 km, and where the ground speed is ~4.2 km/s at closest approach is shown in Fig. 15. To achieve both a high spatial resolution and measure the radiances to the accuracy necessary, and to properly constrain them, requires a nadir pointing accuracy of one tenth of a pixel stable over a 1.0s period. In NF mode, the pixel size is 0.42 mrad, so the instrument requires a relative pointing accuracy of 42 μrad/s. The WF mode pointing requirement is less demanding, as the pixel iFOV is six times wider, which gives a required pointing accuracy of 252 μrad/s.

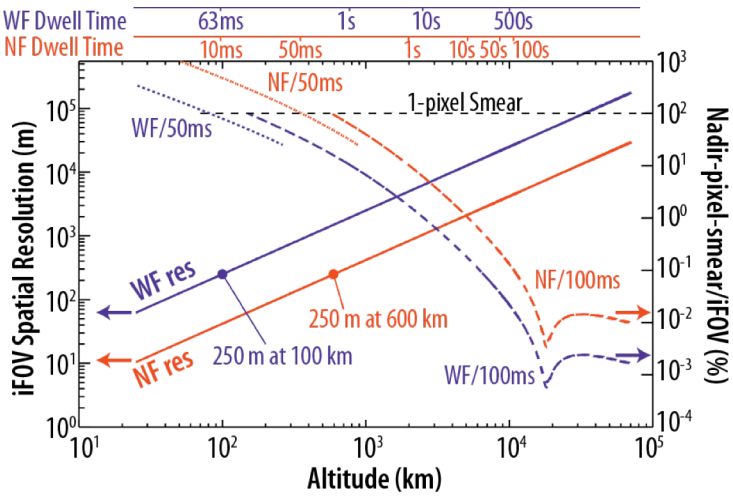

Figure 15. Spatial resolution and nadir pixel smear as a percentage of the iFOV, both as a function of altitude. The pixel smear is typically small, except at closest approach; e.g., for a fly-by ground speed of ~4.4 km/s at 25 km and ~2.4 km/s at 600 km. The dwell time for NF and WF are also given for 1-pixel smear for the full range of altitudes.

Image blurring occurs at nearest approach in the fly-by scenario due to the spacecraft's relative velocity. Fig. 15 shows the percentage by which the NF iFOV (0.42 mrad) and the WF iFOV (2.5 mrad) move during a 0.1s integration when viewing in a typical fly-by. The expected pixel smear is less than 1% for distances >600 km and presents no difficulty for the channels with high SNR (§6.2). During the closest approaches, pixel smearing is countered by appropriate stepping of the source selection mirror during an integration cycle, binning pixels or reducing the integration time.

8. Assessment of performance using the NASA Europa Mission fly-by scenario

As an example of the surface coverage, data volume, sufficiency and flexibility of the dual-telescope radiometer performance consider the planned Europa Clipper Mission [37], in 2020; a fly-by profile that is divided into encounter and non-encounter periods.

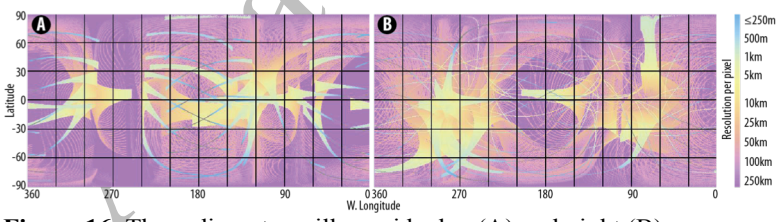

Figure 16. The radiometer will provide day (A) and night (B) observations of Europa's surface. In a fly-by mission, full coverage of the surface is not obtainable so the best resolution obtained across the surface is indicated. Areas in common between (A) and (B) will be observed in both optimal day (9 am to 3 pm) and night (9 pm to 6 am) conditions.

8.1 Surface Coverage

The NF and WF telescopes are designed to be bore-sighted with the spacecraft's nadir-view instrument axis. Using the JPL/Navigation and Ancillary Information Facility data product 13-F7 as a representative trajectory, Fig. 16 depicts (a) the best surface resolutions for optimal daytime observations (*i.e.* between 9 am and 3 pm); and (b) the best surface resolutions for optimal nighttime observations (between 9 pm and 6 am). The radiometers FPA with 5-line 64-pixel arrays provide

full coverage of the surface at lower resolutions along the longitudes of the fly-by ingress and egress. High spatial resolution thermal data is obtained in the intermediate longitudes. The coverage summary chart (Table 7) shows values for all data plus several relevant data subsets (optimal daytime data only, optimal nighttime data only, coverage with daytime and nighttime data). As altitude varies throughout a fly-by, the radiometer produces data with different spatial resolutions. At the smallest scales (≤250 m/pix) the radiometer is able to distinguish common landforms on Europa. Even at ≤1 km/pix, hot spots can be mapped to tectonic or chaotic terrains. At lower resolutions of ≤25 km/pix, large-scale chaos features can be characterized.

Table 7. Surface data coverage at various spatial resolutions calculated for the Europa 13-F7 fly-by trajectories.

	Total Coverage area (10^6 km^2)	%	Daytime Coverage area (km^2)	%	Nighttime Coverage area (km^2)	%	Day/ Night Coverage area (km^2)	%
≤250 m/ pix	55	1.8	37	1.2	34	1.1	38	1.2
≤1 km/pix	266	8.7	162	5.3	110	3.6	147	4.8
≤25 km/ pix	1758	57.4	894	29.2	894	29.2	906	29.6
≤50 km/ pix	2388	78.0	1329	43.4	1632	53.3	1217	39.7
≤150 km/ pix	2869	93.7	1834	59.9	2287	74.7	1398	45.7

8.2 Data Volume and Sufficiency

Assuming 45 fly-bys of the planned 13-F7 trajectory, 16-bit/pixel resolution with a 2:1 compression, and observation times that vary between 0.05s and 1s, the calculated total mission science data volume is ~7 GB. The dual-telescope approach generates sufficient, high-quality data over the 45 fly-bys to span the full range of spatial resolutions on Europa's surface (§6.5). Using both telescopes, the total combined fly-by Europa surface coverage exceeds 95%.

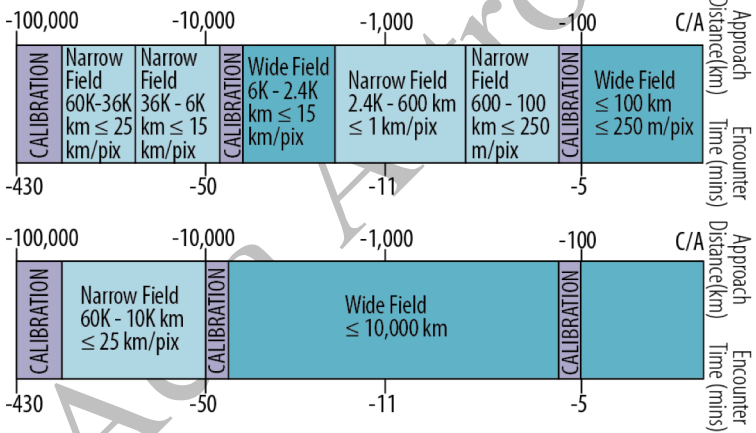

Figure 17. The dual-telescope system adds flexibility to its observation timeline. For example, in the case of the 13-F7 fly-bys for Europa, if the strategy is to prioritize higher resolution data over surface coverage then the observation timeline shown in the top panel is preferred. If the plan is to maximize the surface area covered then the observational timeline shown in the bottom panel is preferred.

8.3 Mission Profile

During the example mission's 45 Europa encounters, the radiometer switches between NF and WF telescope observations, and calibrates using space and the blackbody reference. The instrument's standard encounter timeline (Fig. 17) is applicable to most encounters with minimal modification. For the example baseline Europa profile the radiometer is activated at 60,000 km and the NF telescope is used for most of the encounter period. The WF telescope is used closer in at encounter ranges between 6000-2400 km and <100 km to acquire 15 km/pix and 250 m/pix mapping data, respectively. Long (~1 hr) calibration periods occur prior to encounter, with shorter calibration checks (~1 min) occurring during the switch from NF to WF telescopes.

During non-encounter periods, far from Europa, the NF and WF telescopes are used to observe space, giving a cross-check via the deep space calibration port.

9 Characterizing Compelling Landing Sites with Anomalous Temperatures

At Enceladus, thermal IR imaging with Cassini/CIRS was the most straightforward method of locating surface heat signatures from tectonic features, whereas the active plumes from these features were only visible in high-phase observations of the moon's south polar region [19, 38]. The correlation between the jet sources inferred using Cassini/ISS imaging and the heat signatures seen by CIRS [39] confirmed the anomalously-warm regions were active and likely driven by tidal stresses [40, 41]. Recent Hubble Telescope (HST) observations hint at the possibility Europa may currently be active [42]. The source of activity could either be chaotic terrain or tectonic terrain. Chaotic terrain may form by liquid water lenses beneath the surface [43] disrupting the surface and possibly venting volatiles in the process. Or, volatile release may be linked to fractures, in similar processes as those acting on Enceladus. Cassini/CIRS results helped link Enceladus' eruptions to fractures near its south pole (Fig. 18) using thermal images with resolutions as low as 6 km/pixel laid over visible imaging data [19, 38]. Chaotic features and tectonic terrain on Europa can also be characterized with thermal images on the scale of a few kilometers [44, 45]. The thermal radiometer concept presented here is able to obtain thermal images of Europa's surface at scales of ≤1 km/pixel to supplement visible context images and thereby allow any sites of current or recent activity to be linked to their source structures on the surface (Fig. 19).

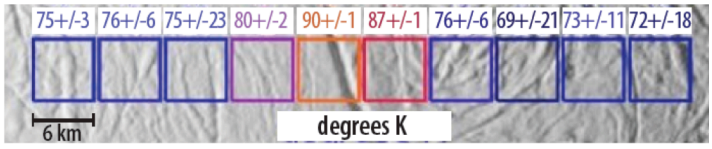

Figure 18. Cassini/CIRS observations constrain Enceladus' current activity to large fractures on its south pole [19]. Fields-of-view of 10 Cassini/CIRS detector pixels (6 km resolution) are overlain on a Cassini/ISS map, showing temperature enhancements near fractures.

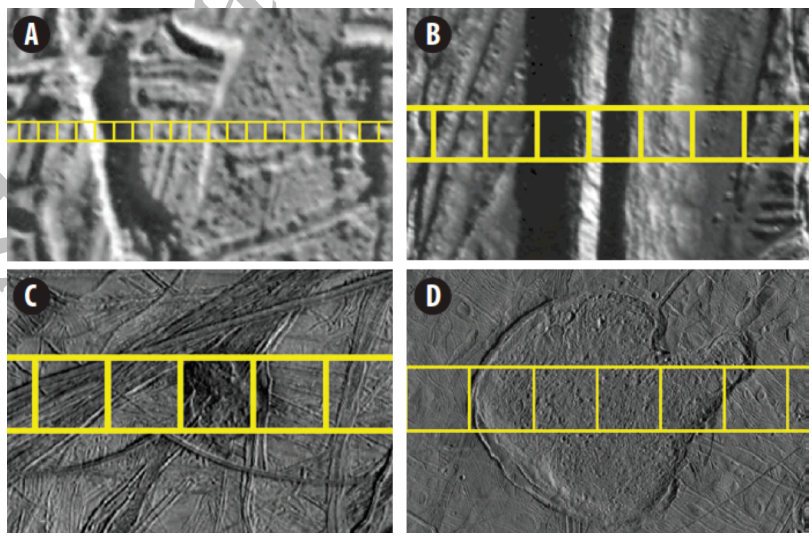

Figure 19. The dual telescope design of the thermal radiometer will provide observations at multiple scales. In panels A-D, a few frames of the thermal radiometer detector over images of Europa's surface to get a sense of the ability of this instrument to correlate its measurements with surface geology are shown. The FOV's are (A) 250 m/pixel, (B) 1 km/pixel, (C) 15 km/pixel and (D) 25 km/pixel.

10 Summary

The dual-telescope thermal infrared radiometer concept described in this paper measures the thermal emission from a cold planetary body surface in order to determine its temperature. Icy surfaces radiate heat as a graybody at temperatures that reflects a balance between insolation and endogenic heat flow. To uniquely determine the surface temperature and emissivity for example of the icy moon Europa (50-300 K), requires thermal emission measurements in five spectral channels: 8-14 μm, 12.5-25 μm, 25-50 μm, 50-100 μm, and 100-200 μm. Using a calibration scheme that includes both deep-space and onboard blackbody source measurements gives an expected radiometric accuracy for the proposed instrument concept of better than 2 K, this level of performance allows subtle differences in thermophysical properties (such as thermal inertia) to be determined. The instrument achieves high spatial resolution, with the ability to obtain measurements of thermal emission at spatial scales ≤250 m/pixel at a range of 600 km. The instrument concept is highly flexible and will be able to address high-priority goals for future fly-by missions to the outer planets, icy moons and primitive bodies in the solar system.

Acknowledgements

We wish to thank the National Aeronautics and Space Administration (NASA) for providing funds through the Instrument Concepts for Europa Exploration Program for Research Opportunities in Space and Earth Sciences (2013), managed by Dr. Curt Niebur, to help mature the thermal radiometer optical design concept and the radiation-hard detector and readout technology presented here. We also wish to thank Carletta Missouri, Brittany Klein and David Palace from NASA, GSFC for providing the graphics.

References

1. Chase, S. C., Ruiz, R. D., Munch, G., Neugebauer, G., Schroeder, M., Trafton, L. M. (1974). Pioneer 10 infrared radiometer experiment : Preliminary results. Science 183, 315-317.
2. Hanel, R., D. Crosby, L. Herath, D. Vanous, D. Collins, H. Creswick, C. Harris, and M. Rhodes, Appl. Opt. 9, 1391, (1980).
3. Reuter, D. A., S. A. Stern, J. Scherrer, D. E. Jennings, J. Baer, J. Hanley, L. Hardaway, A. Lunsford, S. McMuldroch, J. Moore, C. Olkin, R. Parizek, H. Reitsma, D. Sabatke, J. Spencer, J. Stone, H. Throop, J. Van Cleve, G. E. Weigle and L. A. Young, Ralph: A Visible/Infrared Imager for the New Horizons Pluto/Kuiper, Space Science Reviews 140.1-4 (Oct 2008): 129-154
4. Flasar, F.M., V.G. Kunde, M.M. Abbas, R.K. Achterberg, P. Ade, A. Barucci, B. Bezard, G.L. Bjoraker, J.C. Brasunas, S.B. Calcutt, R. Carlson, C.J. Cesarsky, B.J. Conrath, A. Coradini, R. Courtin, A. Coustenis, S. Edberg, S. Edgington, C. Ferrari, T. Fouchet, D. Gautier, P.J. Gierasch, K. Grossman, P. Irwin, D.E. Jennings, E. Lellouch, A.A. Mamoutkine, A. Marten, J.P. Meyer, C.A. Nixon, G.S. Orton, T.C. Owen, J.C. Pearl, R. Prange, F. Raulin, P.L. Read, P.N. Romani, R.E. Samuelson, M.E. Segura, M.R. Showalter, A.A. Simon-Miller, M.D. Smith, J.R. Spencer, L.J. Spilker and F.W. Taylor, Exploring the Saturn System in the Thermal Infrared: The Composite Infrared Spectrometer, Space Sci. Rev., Vol. 115, pp. 169-297, 2004.

5. Hanel, R. A., B. Schlachman, F. D. Clark, C. H. Prokesh, J. B., Taylor, W. M. Wilson, and L. Chaney, Appl. Opt. 9, 1767 (1970).
6. Hanel, R. A., B. Schlachman, D. Rodgers, and D. Vanous, Appl. Opt. 10, 1376 (1971).
7. Hanel, R. A., B. Schlachman, E. Breihan, R. Bywaters, F. Chapman, M. Rhodes, D. Rodgers, and D. Vanous, Appl. Opt. 11, 2625 (1972).
8. McCleese, D. J., J. T. Schofield, F. W. Taylor, S. B. Calcutt, M. C. Foote, D. M. Kass, C. B. Leovy, D. A. Paige, P. L. Read, and R. W. Zurek (2007), Mars Climate Sounder: An investigation of thermal and water vapor structure, dust and condensate distributions in the atmosphere, and energy balance of the polar regions, J. Geophys. Res.,112, E05S06, doi:10.1029/2006JE002790.
9. Paige, D. A., M.C. Foote, B.T. Greenhagen, J.T. Schofield, S. Calcutt, A.R. Vasavada, D.J. Preston, F.W. Taylor, C.C. Allen, K.J. Snook, B.M. Jakosky, B.C. Murray, L.A. Soderblom, B. Jau, S. Loring, J. Bulharowski, N.E. Bowles, I.R. Thomas, M.T. Sullivan, C. Avis, E.M. De Jong, W. Hartford, D.J. McCleese, The Lunar Reconnaissance Orbiter Diviner Lunar Radiometer Experiment, Space Sci. Rev., DOI 10.1007/s11214-009-9529-2, published online: 26 June 2009
10. Hiesinger, H., J. Helbert and MERTIS Co-I Team, The Mercury Radiometer and Thermal Infrared Spectrometer (MERTIS) for the BepiColombo mission, Planetary and Space Science, Vol. 58, Issues 1-2, January 2010, pp. 144-165
11. Lakew, B., S. Aslam, and JETS Co-I Proposal Team, "JETS - Jupiter Europa Thermal Sounder," NASA Goddard Space Flight Center, Instrument Development Study 2011, (abstract available on request)
12. Irwin, P.G. J., Ellison, B. N., de Kok, R., Teanby, N. A., Calcutt, S. B., Alderman, B., Oxford RAL Terahertz-Infrared Sensor – ORTIS, European Planetary Science Congress 2008, Proceedings of the conference held 21-25 September, 2008 in Münster, Germany
13. Irwin, P. G., S. Aslam and JSTIM Co-I Team, "JSTIM - Jupiter System Thermal Infrared Mapper," Proposal submitted in response to ESA's Announcement Opportunity for the JUICE Payload, 2012, (abstract available on request)
14. Aslam, S., T. Hurford and TIMER Co-I Team, "TIMER - Thermal Imager for Europa Reconnaissance - Technology Maturation and Risk Mitigation" NASA Goddard Space Flight Center, ICEE Study 2011, (abstract available on request)
15. Hurford, T., S. Aslam, and TIMERS Co-I Team, "TIMERS - Thermal Imager for Europa Reconnaissance and Science," A Europa Proposal Submitted in response to AO# NNH12ZDA006O-EUROPA, 2014 (abstract available on request)
16. Goldstein, B., Pappalardo, R., Cooke, B., Magner. T., Prockter, L., Senske, D., Europa Clipper Update, OPAG, Jan. 13, 2014 (online: http://www.lpi.usra.edu/opag/jan2014/presentations/9_Clipper.pdf)
17. Vision and Voyages for Planetary Science in the Decade 2013-2022, The National Academies Press (online: http://www.nal.edu/catalog.php?record_id=13117)
18. Planetary Science Decadal Survey, Io Observer, Mission Concept Study (online: http://sites.nationalacademies.org/cs/groups/ssbsite/documents/webpage/ssb_059314.pdf)
19. Spencer, J. R., J. C. Pearl, M. Segura, F. M. Flasar, A. Mamoutkine, P. Romani, B. J. Buratti, A.R. Hendrix, L. J. Spilker, and R. M. C. Lopes (2006), "Cassini Encounters Enceladus: Background and the Discovery of a South Polar Hot Spot," Science, 311, 1401S.
20. Howett, C. J., J. R. Spencer, P. Schenk, R.E. Johnson, C. Paranicas, T.A. Hurford, A. Verbiscer and M. Segura (2011), "A high-amplitude thermal inertia anomaly of probable magnetospheric origin on Saturn's moon Mimas," Icarus 216, 221-226.
21. Hanel, R.A., Conrath, B.J., Jennings, D.E., Samuelson, R.E., "Exploration of the Solar System by Infrared Remote Sensing," Book, Cambridge University Press, Second edition 2003.
22. Mellon, M. T., R. L. Fergason, and N. E. Putzig (2008), "The Thermal Inertia of the Surface of Mars," in The Martian Surface: Composition, Mineralogy, and Physical Properties, Cambridge Planetary Science edited by J. F. Bell III, p. 399–427, Cambridge Univ. Press, Cambridge, UK.

23. Spencer, J. R. L. K. Tamppari, T. Z. Martin, and L. D. Travis (1999), "Temperatures on Europa from Galileo Photopolarimeter-Radiometer: Nighttime Thermal Anomalies," Science, 284, 1514.
24. Howett, C. J. A., J. R. Spencer, J. Pearl, and M. Segura (2010), "Thermal inertia and bolometric Bond albedo values for Mimas, Enceladus, Tethys, Dione, Rhea and Iapetus as derived from Cassini/CIRS measurements," Icarus, 206, 573–593.
25. Rathbun, J. A., N. J. Rodriguez, and J. R. Spencer (2010), "Galileo PPR observations of Europa: Hotspot detection limits and surface thermal properties," Icarus, 210, 763.
26. http://www.ipht-jena.de/en/home.html
27. Aslam, S., A. Akturk, G. Quilligan, "A Radiation Hard Multi-Channel Digitizer ASIC for Operation in the Harsh Jovian Environment," Book Chapter in Extreme Environment Electronics, Ed. J. D. Cressler, H. A. Mantooth, CRC Press, Boca Raton, FL, Nov. 2012, ISBN: 978-1-4398-7430-1.
28. Quilligan, G., S. Aslam, B. Lakew, J. DuMonthier, R. Katz and I. Kleyner, "A 0.18.m CMOS Thermopile Readout ASIC Immune to 50 Mrad Total Ionizing Dose (Si) and Single Event Latchup to 174 MeV-cm2/mg," International Workshop on Instrumentation for Planetary Missions (IPM-2014), November 2014, Greenbelt, MD 20771.
29. Thermal Infrared Sensor (TIRS), http://landsat.gsfc.nasa.gov/?p=5474
30. Hawkins, G., et al., Infrared Physics & Technology 39 (1998) 297-306.
31. Hawkins, G., et al., Infrared Physics &Technology 45 (2004) 69-79.
32. Foote, M.C., "Temperature stabilization requirements for unchopped thermal detectors," http://trsnew.jpl.nasa.gov/dspace/bitstream/2014/17051/1/99-0472.pdf.
33. Aslam, S., Quilligan, G., ICEE report private communication, 2014.
34. Gomez-Elvira, J., et al., "REMS: The Environmental Sensor Suite for the Mars Science Laboratory Rover," Space Sci Rev, 2012, DOI 10.1007/s11214-012-9921-1.
35. Becker, W., et al., "Black Gold Deposits as Absorbers for Far Infrared Radiation," phys. stat. sol. (b)194, 241 (1996).
36. Tremblay, P., et al., "Pixel-wise real-time advanced calibration method for thermal infrared cameras," Infrared Imaging Systems: Design, Analysis, Modeling, and Testing XXI, edited by Gerald C. Host, Keith A. Krapels, Proc. of SPIE Vol. 7662, 766212, 2010.
37. JPL/Navigation and Ancillary Information Facility data product 13-F7
38. Porco, C. C., P. Helfenstein, P. C. Thomas, A. P. Ingersoll, J. Wisdom, et al., "Cassini observes the Active South Pole of Enceladus," Science, 311, 1393P, 2006.
39. Spitale, J. N., and C. C. Porco, "Association of the jets of Enceladus with the warmest regions on its south-polar fractures," Nature, 449, 695, 2007.
40. Hurford, T. A., P. Helfenstein, G. V. Hoppa, R. Greenberg, and B. G. Bills, "Eruptions arising from tidally controlled periodic openings of rifts of Enceladus," Nature, 447, 272, 2007.
41. Hurford, T. A., P. Helfenstein, J. N. Spitale, "Tidal control of jet eruptions on Enceladus as observed by Cassini ISS between 2005 and 2007," Icarus 220, 896, 2012.
42. Roth, L., J. Saur, K. D. Retherford, D. F. Strobel, P. D. Feldman, M. A., McGrath, and F. Nimmo, "Transient Water Vapor at Europa's South Pole," Science, 343, 171, 2014.
43. Schmidt, B. E., D. D. Blankenship, G. W. Patterson, and P. M. Schenck, "Active formation of 'chaos terrain' over shallow subsurface water on Europa," Nature, 479, 502, 2011.
44. Kattenhorn, S. A., and T. A. Hurford, "Tectonics of Europa," Chapter in the book Europa edited by Pappalardo, Mckinnon and Khurana, The University of Arizona Press, ISBN 978-0-8165-2844-8, 2009.
45. Neish, C. D., L. M. Prockter, and G. W. Patterson, "Observational constraints on the identification and distribution of chaotic terrain on icy satellites," Icarus, 221, 72N, 2012.